# Ultralong lifetime for fully photogenerated spin-polarized current in two-dimensional ferromagnetic/nonmagnetic semiconductor heterostructures

Zhaobo Zhou,[1,*] Xiwen Zhang,[1,2,*] Yilv Guo,[1] Yehui Zhang,[1] Xianghong Niu,[3] Liang Ma,[1,†] and Jinlan Wang[1,‡]
[1]*School of Physics, Southeast University, Nanjing 211189, China*
[2]*School of Mechanical Engineering, Southeast University, Nanjing 211189, China*
[3]*New Energy Technology Engineering Laboratory of Jiangsu Province & School of Science, Nanjing University of Posts and Telecommunications (NJUPT), Nanjing 210023, China*

(Received 27 February 2021; accepted 14 May 2021; published 9 June 2021)

Photogenerated fully spin-polarized current has attracted considerable attention in spintronics owing to its high efficiency for information processing but low energy consumption. However, the short spin carrier lifetime of the primary materials significantly impedes the practical application of spin-polarized current and presents a major challenge. Here, on the basis of density functional theory and nonadiabatic molecular dynamics simulations, we design two prototypes of two-dimensional (2D) ferromagnetic/nonmagnetic semiconductor heterostructures ($CrI_3/MoSe_2$ and $CrBr_3/MoS_2$) with demonstrated ultralong photogenerated spin carrier lifetime. It is shown that the photogenerated spin holes can be effectively injected from the ferromagnetic layer to the nonmagnetic layer, and fully spin-polarized electrons will be confined in the ferromagnetic layer due to their type-II spin-polarized channel and large spin-flip gap. More surprisingly, the photogenerated spin carrier lifetime of these heterostructures is up to the time scale of nanoseconds. Such an ultralong spin carrier lifetime is mainly originated from small nonadiabatic coupling induced by weak spin electron-phonon interaction and slow nuclear velocity. Our results provide insights into the design of 2D semiconductor spintronic devices with an ultralong fully spin-polarized current lifetime.

DOI: 10.1103/PhysRevB.103.245411

## I. INTRODUCTION

The spin degree of freedom of electrons has long been ignored in prevailing charge-based electronics. The discovery and successful application of giant magnetoresistance [1,2] as a high-density and high-speed data storage device is one of the very limited well-known examples of exploiting the spin degree of freedom. Continuous efforts have been devoted in recent decades for developing high-efficiency spintronic devices [3–6] due to their expected high data processing speed, ultralow power consumption, and high integration density [7–10]. Naturally, the generation of fully spin-polarized current has become one of the most important topics in spintronics research. In terms of the efficiency and energy consumption, the optical excitation has been proposed as an ideal scheme for generating the fully spin-polarized current [4,11–13]. On the one hand, the optical response of spin carriers typically occurs in the time scale of femtoseconds, which is much more sensitive than the optoelectronic response. On the other hand, the photogenerated spin-polarized current could avoid the generation of Joule heat induced by the resistance of traditional ferromagnetic (FM) metal or half metal (e.g., Co, Ni, $Fe_3O_4$, $CrO_2$) [9,14,15]. Despite the above-mentioned advantages, the carrier lifetime of photogenerated fully spin-polarized current in common ferromagnetic metal or half-metal materials is rather short, which significantly limits the subsequent spin injection, manipulation, and detection. In this sense, ferromagnetic semiconductor materials are highly desirable since the spin-polarized carriers can survive for much longer time in this type of materials [16].

Upon the coming of the post-Moore era, two-dimensional (2D) semiconductor materials have been widely studied with the great promise of numerous advanced electronic applications [17–20]. Unfortunately, the nonmagnetic nature of most 2D semiconductors has hampered their applications in spintronics. In light of the common advantages of 2D materials, if ferromagnetism can be induced in 2D semiconductors, they are expected to become potential high-performance spintronics materials. Several traditional methods including doping of magnetic metal atoms (e.g., Mn, Fe, Co, and Ni), creating vacancy, strain, and annealing under different atmospheres, have been used to acquire ferromagnetism in 2D semiconductors [21–27]. Nevertheless, these strategies either failed or achieved very limited success in practical application. First, doping-induced ferromagnetism is unstable and susceptible to the environment and structural deformation [28]. Second, the introduced spin energy states are mostly localized near the Fermi level, which enables the rapid recombination between the photogenerated spin electrons and holes in the time scale of picoseconds [29]. It is exciting that intrinsic 2D FM semiconductors have been discovered very recently, including the $CrX_3$ ($X$ = Cl, Br, I) monolayer and $Cr_2Ge_2Te_6$ bilayer [30–32]. Their suitable band gap and large

*These authors contributed equally to this work.
†Corresponding author: liang.ma@seu.edu.cn
‡Corresponding author: jlwang@seu.edu.cn

 ©2021 American Physical Society

spin-flip gap are feasible to generate photogenerated fully spin-polarized carriers and delay their annihilation under unpolarized light with a specific frequency. Such a momentous discovery provides a new playground for applications of 2D FM semiconductors for spintronics at the nanoscale [33]. However, the photogenerated spin carriers are still localized on FM semiconductors, suggesting their limited spin carrier lifetime. Therefore, exploring an effective strategy to further prolong the photogenerated spin carrier lifetime is thus desired.

For traditional nonmagnetic (NM) 2D semiconductors, constructing van der Waals heterostructures with type-II band alignment has been demonstrated to be an effective method to rapidly separate the photoexcited electrons and holes. The formed indirect excitons in a heterostructure always show a longer lifetime than that of direct excitons in individual layers [34–40]. For instance, Frank *et al.* observed that the signal of transient absorption measurements in the $MoS_2/MoSe_2$ heterostructure is about ten times longer than that of the $MoSe_2$ monolayer [34]. Using time-domain density functional theory (DFT), Long *et al.* found that the electron-hole (*e*-h) recombination lifetime of the $MoS_2/MoSe_2$ heterostructure is one order of magnitude longer than that of the isolated $MoS_2$ or $MoSe_2$ monolayer as well [38]. Enlightened by these resports, a reasonable question arises in our minds. Can we promote the spin carrier lifetime significantly by constructing a 2D FM/NM semiconductor heterostructure with type-II band alignment? In such a 2D heterostructure, the photogenerated spin electrons and holes are expected to be efficiently separated by being injected from the FM layer to the NM layer. Such a smart strategy is feasible in principle but has rarely been explored.

To validate this idea, we design a prototype of 2D FM/NM semiconductor heterostructures by combining DFT calculations and nonadiabatic molecular dynamics (NAMD) simulations. In our scheme, the photogenerated spin holes will be rapidly injected from a 2D $CrX_3$ ($X$ = I, Br) FM layer to a 2D $MoY_2$ ($Y$ = S, Se) NM layer while fully spin-polarized electrons will reside in $CrX_3$ due to their large spin-flip gap and type-II spin-up channel. As expected, the photogenerated spin carrier lifetime of the designed 2D FM/NM semiconductor heterostructure has been significantly improved by one to two orders of magnitude compared with the isolated 2D FM $CrX_3$ component. Further analysis reveals that such ultralong photogenerated spin carrier lifetime is closely related to the small wave function overlap of donor-acceptor states and unique low-frequency vibrational modes, which leads to weak electron-phonon (*e*-ph) interaction and slow nuclear motion. Importantly, by cleverly utilizing the 2D NM semiconductor as the spin carrier trap layer, this strategy not only provides a route for overcoming the issue of short spin-polarized current lifetime in 2D FM semiconductors but also may enable many advanced applications.

## II. COMPUTATIONAL METHODS

All calculations of geometric relaxation and electronic structure, as well as *ab initio* molecular dynamics, were explored using VASP [41,42]. The Perdew-Burke-Ernzerhof (PBE) was used to treat the electron exchange-correlation functional based on the framework of generalized gradient approximation (GGA) [43]. The projector-augmented wave (PAW) method was utilized to describe the electron-ion interaction and single-particle wave functions were expanded into a plane-wave basis up to a cutoff energy of 500 eV [44]. The lattice constants and electronic structure were optimized using a Monkhorst-Pack $k$ mesh of $5\times5\times1$ grid and a convergence threshold was $10^{-5}$ eV for energy and 0.02 eV $Å^{-1}$ for force, respectively. The van der Waals weak interaction was induced using the semiempirical correction scheme of Grimme, DFT-D3 [45]. Also, HSE06 hybrid functional [46] was utilized to obtain a more accurate band structure. A vacuum region of at least 20 Å along the $z$ direction was used to avoid the interaction between two neighboring periodic units.

The photogenerated spin *e*-h recombination and spin hole injection dynamics were calculated by using NAMD simulations, as implemented in the PYXAID code [47,48]. The decoherence-induced surface hopping (DISH) method within time-domain density functional theory was carried out [49]. After lattice optimization at 0 K, both of the models were warmed up to 300 K during 4 ps in the canonical ensemble through repeated velocity rescaling. Next, 4 ps *ab initio* molecular dynamics (AIMD) was calculated in the microcanonical ensemble with a 1 fs nuclear time step, and following NAC calculations were carried out along this AIMD trajectory. The 200 initial configurations were selected randomly in the first 1 ps AIMD trajectory. Then 3 ps NAMD simulations were performed to obtain the state population of excited spin carriers.

## III. RESULTS AND DISCUSSION

### A. Design strategy and modeling

To obtain photogenerated fully spin-polarized carriers and long spin carrier lifetime, a large spin-flip gap and suitable band gap in the FM semiconductor and type-II band alignment are the prerequisites for the design of the targeted 2D FM/NM heterostructure, as shown in Fig. 1(a). First, a large spin-flip gap and suitable band gap are favored to excite carriers of a single spin channel, which will generate fully spin-polarized *e*-h pairs under photoexcitation with appropriate energy [50]. Second, type-II band alignment facilitates the injection of photogenerated spin carriers from the FM layer to the NM layer, which has been demonstrated in spin solar cells and spin photodiodes [4]. Recently, $CrI_3$ and $CrBr_3$ monolayers [Fig. 1(b)] have been demonstrated to be intrinsic 2D FM semiconductor in both experiment and theory [30,31,51,52]. More importantly, their suitable band gap and large spin-flip gap offer an opportunity to utilize them to generate fully spin-polarized current [51,53,54]. We choose 2H-$MoS_2$ and $MoSe_2$ monolayers [Fig. 1(b)] as NM layers for the 2D FM/NM heterostructure because of their high spin-to-charge conversion efficiency; thus any signal from $MoS_2$ or $MoSe_2$ implies that the spin carrier has been injected across the interface [15,55]. Furthermore, their good lattice match with $CrBr_3$ and $CrI_3$ (see the Supplemental Material [56] for details) and the smooth and atomically thin heterointerface ensure their chemical and structural stability [57]. Thereby, four heterostructures, $CrI_3/MoSe_2$, $CrBr_3/MoSe_2$, $CrI_3/MoS_2$ and

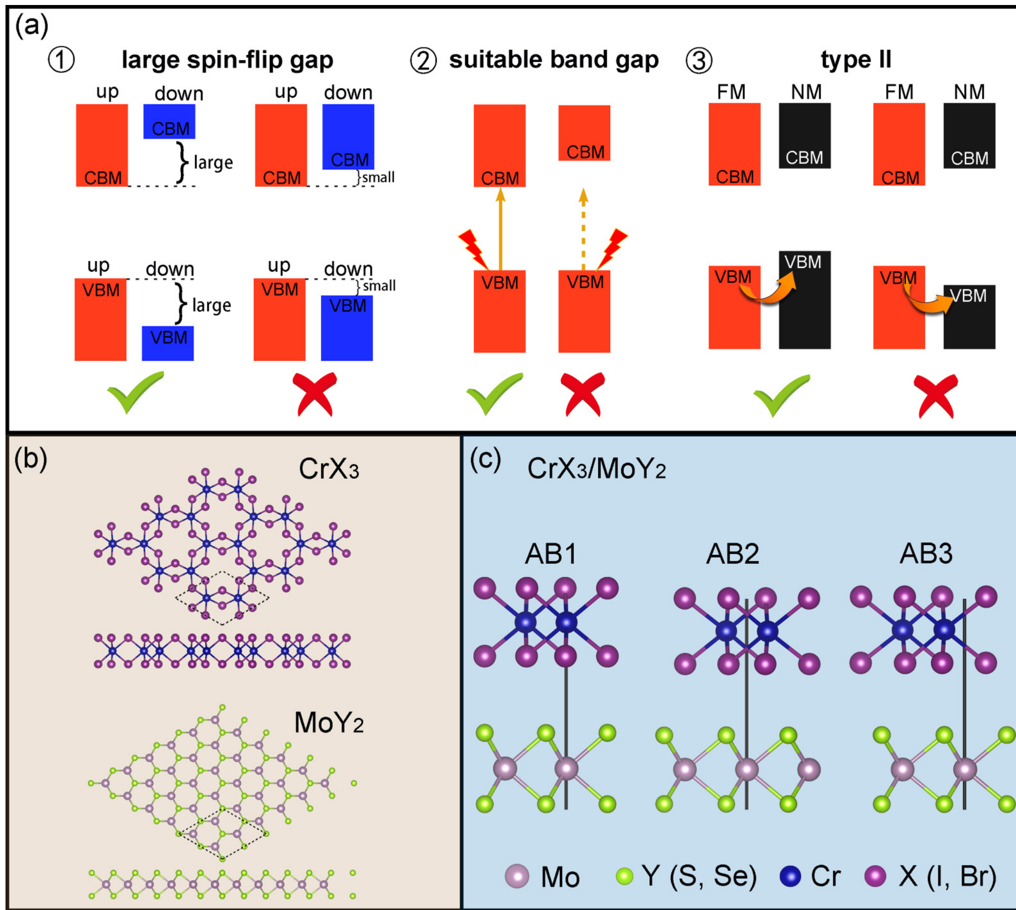


FIG. 1. (a) Schematic diagrams of three favorable conditions for generating and improving photogenerated fully spin-polarized carrier lifetime: (1) large spin-flip gap, (2) suitable band gap, and (3) type-II band alignment. FM and NM represent ferromagnetic and nonmagnetic semiconductor, respectively. (b) Top and side views of $CrX_3$ ($X$ = I, Br) and $MoY_2$ ($Y$ = S, Se) monolayers, and (c) $CrX_3/MoY_2$ heterostructures with AB1, AB2, and AB3 stacking configurations. The pink, green, blue, and violet balls represent Mo, $Y$ (S, Se), Cr, and $X$ (I, Br) atoms, respectively. The black vertical lines are marked to identify the different stacking configurations.

$CrBr_3/MoS_2$, are constructed and considered as appropriate candidates for 2D FM/NM semiconductor heterostructures.

We consider three possible stacking patterns, labeled as AB1, AB2, and AB3, for these four heterostructures, as shown in Fig. 1(c). The calculated ferromagnetic and antiferromagnetic (AFM) energies are listed in Table S1 of the Supplemental Material [56] and the FM state of AB2 stacking has the lowest energy. The band structures of four heterostructures with the lowest energy are shown in Fig. S1 of the Supplemental Material [56]. In particular, the photogenerated spin $e$-h pairs cannot be separated effectively in the $CrI_3/MoS_2$ heterostructure due to its type-I spin-up channel. This could be attributed to the large lattice mismatch (4.6%) between the $MoS_2$ monolayer and the $CrI_3$ monolayer, which induces large lattice strain and significantly changes the band-edge position. In addition, the smallest interlayer band gap for $CrBr_3/MoSe_2$ is harmful to obtain a long interlayer spin carrier lifetime [58,59]. Therefore, we take the $CrI_3/MoSe_2$ and $CrBr_3/MoS_2$ with AB2 stacking as examples for further calculations. Note that the band gap is always underestimated by the PBE functional. To obtain a more accurate band alignment of $CrI_3/MoSe_2$ and $CrBr_3/MoS_2$ heterostructures, we also performed band-structure calculation using the HSE06 functional, as shown in Fig. S2 of the Supplemental Material [56]. Clearly, two heterostructures still present the type-II spin-up channel, indicating that our results are reliable with different calculation methods.

### B. Electronic structure

Before NAMD simulations, we calculate the band structures of $CrI_3/MoSe_2$ and $CrBr_3/MoS_2$ heterostructures with a $3\times3$ supercell to analyze the effect of electronic structure on spin carrier transfer dynamics, as shown in Fig. 2. Both of them possess type-II band alignment in the spin-up channel but type-I band alignment in the spin-down channel. Meanwhile, the observed large spin-flip gaps (0.7 eV for $CrI_3$ and 1.29 eV for $CrBr_3$) provide the driving force to generate fully spin-polarized carriers. That is, under pump light irradiation with appropriate energy, single spin-up electrons can be excited. After that, the photogenerated spin-up electrons would reside in the $CrI_3$ or $CrBr_3$ monolayer while spin-up holes would rapidly be injected into the $MoSe_2$ or $MoS_2$ layer through the type-II spin-up channel. This is expected to cause the effective separation of photogenerated spin $e$-h pairs. In addition, the spin carrier injection efficiency depends on the

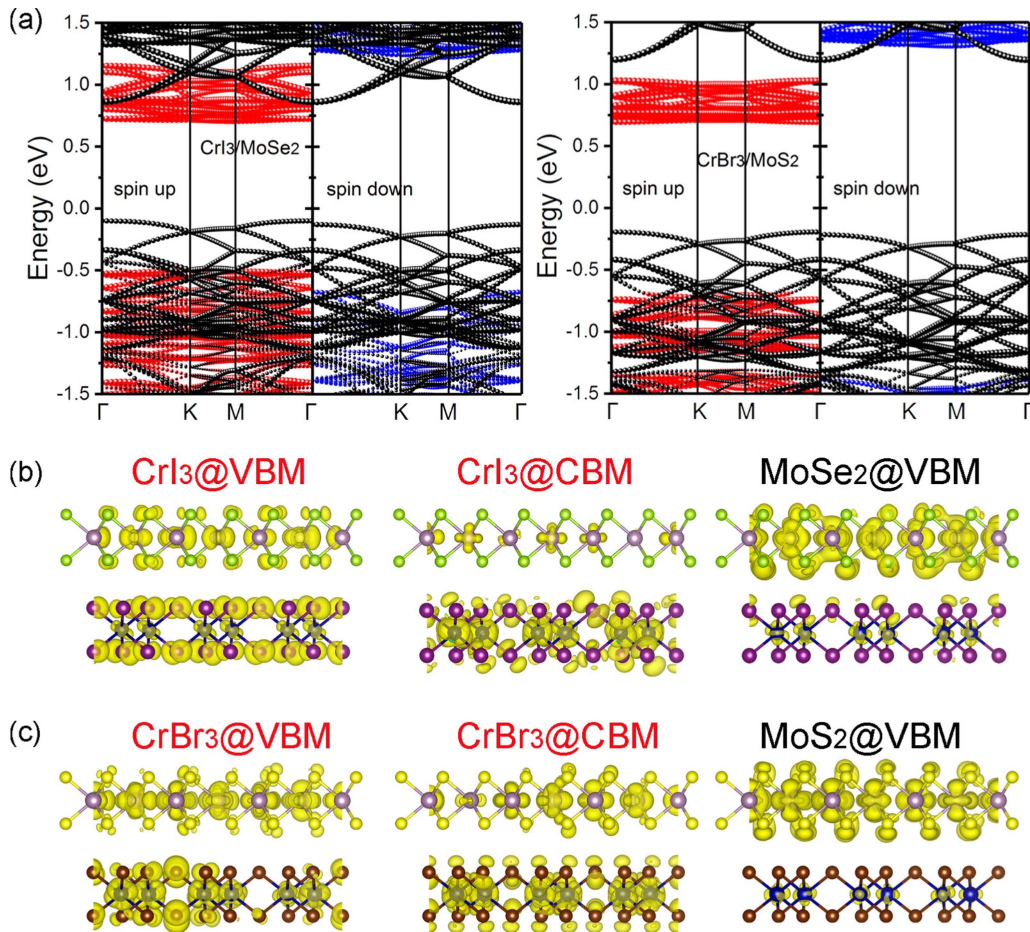


FIG. 2. (a) Band structure of $CrI_3/MoSe_2$ (left) and $CrBr_3/MoS_2$ (right) heterostructures. The blue and red spheres represent spin-up and spin-down channels for $CrI_3$ and $CrBr_3$, respectively. (b), (c) Corresponding charge density of CBM and VBM of $CrI_3/MoSe_2$ and $CrBr_3/MoS_2$ heterostructures, respectively.

donor-acceptor states coupling between FM and NM layers as well. The charge density distributions of the key electronic states for $CrI_3/MoSe_2$ and $CrBr_3/MoS_2$ heterostructures are shown in Figs. 2(b) and 2(c). Clearly, the hole acceptor states ($MoSe_2$@VBM and $MoS_2$@VBM) are mainly localized on the $MoSe_2$ or $MoS_2$ monolayer. Fortunately, the hole donor states ($CrI_3$@VBM and $CrBr_3$@VBM) are delocalized over the whole system. This charge density distribution gives rise to strong donor-acceptor coupling, and highly efficient spin hole injection is expected to occur in these two heterostructures.

When the spin hole injection occurs, the excited spin electrons in the FM layer will recombine with the spin holes in the NM layer. For the $CrI_3/MoSe_2$ heterostructure, the charge densities of initial states ($CrI_3$@CBM) and final states ($MoSe_2$@VBM) are strongly localized on $CrI_3$ and $MoSe_2$, respectively, which exhibit negligible spatial overlap of the donor-acceptor states. Accordingly, the weak donor-acceptor interaction will lead to the recombination of electrons and holes in the same spin-polarized channel very slowly, namely, by slow spin *e*-h recombination. Note that the electron donor state, $CrBr_3$@CBM, is also slightly contributed by $MoS_2$. Such a distribution will enhance the donor-acceptor interaction and accelerate spin *e*-h recombination. Therefore, we infer that the spin carrier lifetime of $CrI_3/MoSe_2$ would be longer than that of $CrBr_3/MoS_2$.

### C. Photogenerated spin carrier dynamics

Based on the type-II spin-up channel of $CrI_3/MoSe_2$ and $CrBr_3/MoS_2$ heterostructures, three significant photogenerated spin carrier dynamics processes should be considered [see Fig. 3(a)]: (1) spin hole injection from FM layer to NM layer; (2) interlayer spin *e*-h recombination at the interface, and (3) intralayer spin *e*-h recombination in the FM layer. These processes occur in parallel and compete with each other, which are similar to the charge separation and *e*-h recombination in traditional semiconductor heterostructures [38,59–61]. If process 1 exhibits a much smaller time scale than that of processes 2 and 3, the spin hole will effectively inject from FM layer to NM layer and process 2 plays a key role in improving spin carrier lifetime. Otherwise, process 3 determines the spin carrier lifetime.

To further characterize the spin hole injection and spin *e*-h recombination dynamics processes, the state population of excited spin carriers of $CrI_3/MoSe_2$ and $CrBr_3/MoS_2$ heterostructures are calculated using NAMD simulations and displayed in Fig. 3. It can be seen that picosecond-scale

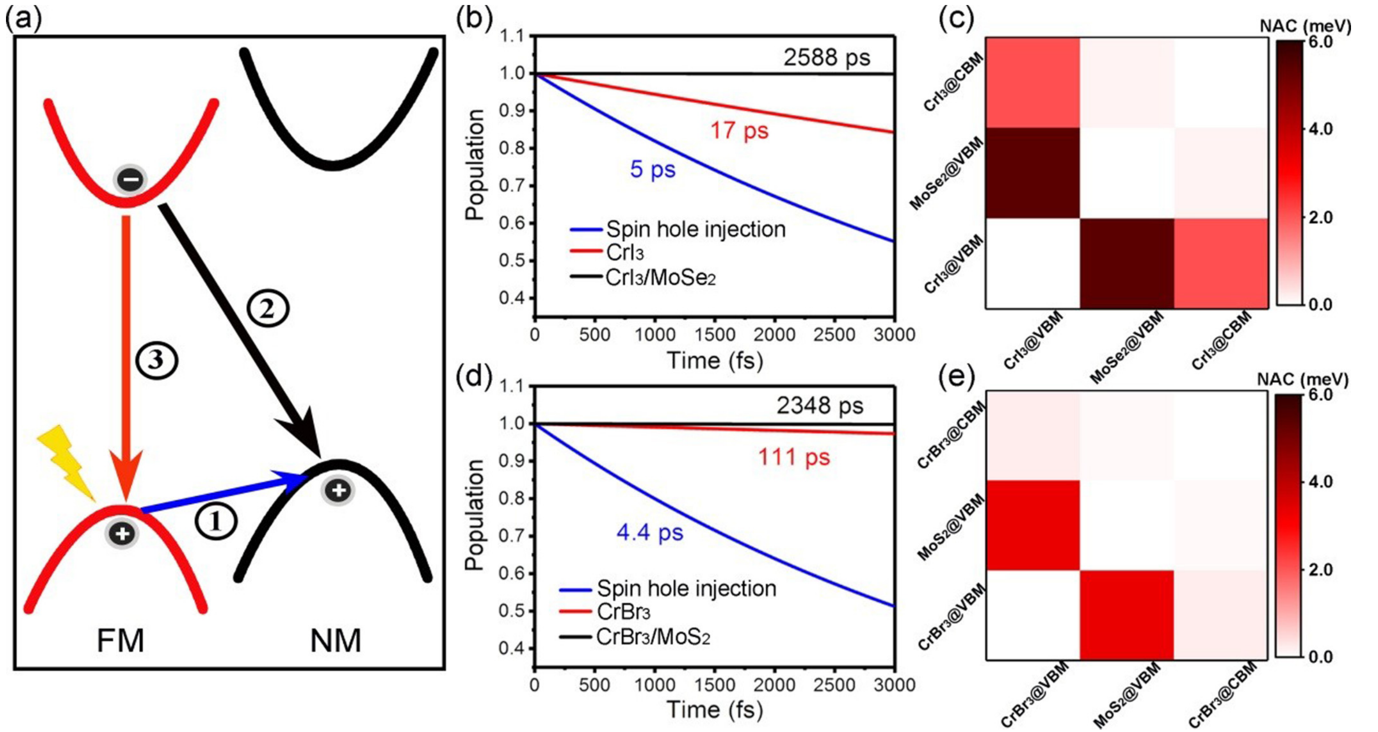


FIG. 3. (a) Schematic image of photogenerated spin carrier dynamics processes: (1) spin hole injection, (2) interlayer spin $e$-h recombination, and (3) intralayer spin $e$-h recombination. (b), (d) State population of the above three dynamics processes in $CrI_3/MoSe_2$ and $CrBr_3/MoS_2$ heterostructures. All data are fitted by the exponential function $f(t) = \exp(-t/\tau)$. (c), (e) The average nonadiabatic coupling (NAC) value between the donor and acceptor states. The larger the NAC, the stronger the coupling.

spin hole injection occurs in both heterostructures while the spin electron at the conduction band minimum (CBM) of the $CrI_3$ and $CrBr_3$ layer recombines with the spin hole at the valence band maximum (VBM) of the $MoSe_2$ and $MoS_2$ layer within a time scale of a few nanoseconds. Such a huge time-scale difference reveals that once the spin hole injects into the NM layer, it is time consuming for the spin electron to recombine with it. Besides, the intralayer spin $e$-h recombination occurs within 111 ps for $CrBr_3$ and 17 ps for $CrI_3$, also much slower than the spin hole injection by a factor of 25.2 and 3.4, respectively. The ultraslow interlayer spin $e$-h recombination leads to an ultralong lifetime of spin-polarized current in $CrI_3/MoSe_2$ and $CrBr_3/MoS_2$ heterostructures. Furthermore, compared with that in $CrBr_3$, the faster intralayer spin $e$-h recombination in $CrI_3$ implies a worse capability to form interlayer spin $e$-h pairs in the $CrI_3/MoSe_2$ heterostructure since more spin electrons will recombine with spin holes through intralayer recombination. As a result, although the spin hole injection rate shows no obvious discrepancy in both $CrI_3/MoSe_2$ and $CrBr_3/MoS_2$ heterostructures, the quantum yield of spin-polarized electrons of the former would be less than that of the latter due to the faster intralayer recombination. In addition, we take the interlayer spin carrier recombination of the $CrI_3/MoSe_2$ heterostructure as an example to probe the effect of initial relaxation on the recombination dynamics, as shown in Fig. S3 of the Supplemental Material [56]. It can be seen that the relaxation of excited electrons at CBM+2 to the CBM (the band edge) can occur within a few picoseconds, indicating that the initial relaxation to the band edge is very fast compared to the recombination dynamics. More importantly, the recombination lifetime is still up to 2108 ps, which is close to that from CBM to VBM (2588 ps), indicating that the impact of the initial relaxation on the recombination dynamics is not obvious.

Similar to traditional charge separation and $e$-h recombination [29,38,62], the spin injection and spin $e$-h recombination are strongly dependent on the averaged nonadiabatic coupling (NAC) element between the key states, which can be expressed as

$$d_{jk} = \langle \varphi_j | \frac{\partial}{\partial t} | \varphi_k \rangle = \frac{\langle \varphi_j | \nabla_R H | \varphi_k \rangle}{\varepsilon_k - \varepsilon_j} \dot{R}. \quad (1)$$

Here $H$ is the Kohn-Sham Hamiltonian, $\varphi$ and $\varepsilon$ are the wave function and eigenvalue, respectively, $R$ is the velocity of the nucleus, and $k$ and $j$ represent different electronic states [63,64]. It is shown in Figs. 3(c) and 3(e) that the NAC between $CrI_3$@CBM ($CrBr_3$@CBM) and $MoSe_2$@VBM ($MoS_2$@VBM) is much smaller than that between $CrI_3$@VBM and $MoSe_2$@VBM, which is responsible for the ultra-long spin carrier lifetime and fast spin hole injection rate in both heterostructures. Also, the NAC between CBM and VBM in $CrBr_3$ is smaller than that of $CrI_3$, further demonstrating the faster spin $e$-h recombination in $CrI_3$ (see Fig. 3). All NAC analyses are consistent with the obtained state population results. According to Eq. (1), the NAC value is determined by the $e$-ph coupling term $\langle \varphi_j | \nabla_R H | \varphi_k \rangle$, energy difference $\varepsilon_k - \varepsilon_j$, and nuclear velocity $\dot{R}$. In general, larger $e$-ph coupling, smaller energy diference, and faster nuclear velocity lead to larger NAC, which accelerates spin

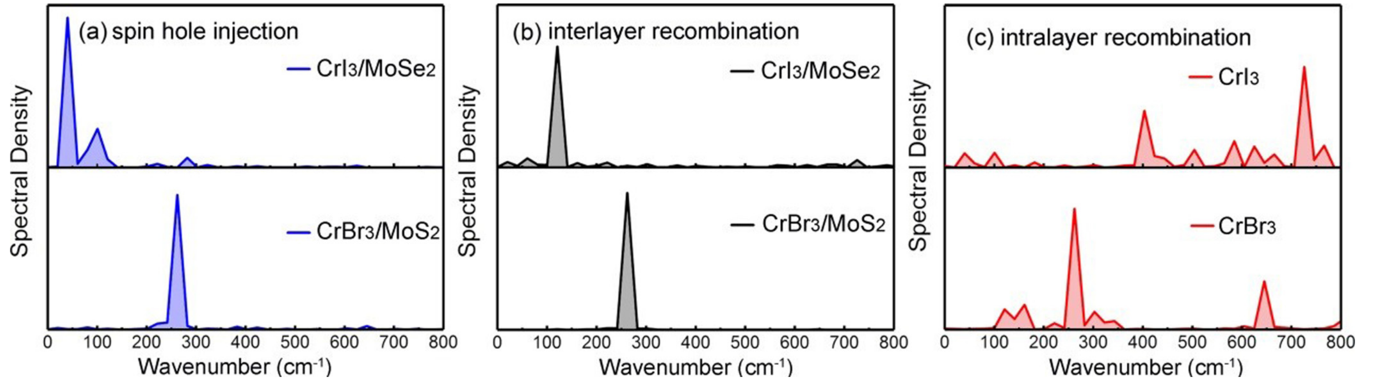


FIG. 4. Spectral densities characterizing phonon modes involved in (a) spin hole injection and (b) interlayer spin *e*-h recombination of $CrI_3/MoSe_2$ and $CrBr_3/MoS_2$ heterostructures and (c) intralayer spin *e*-h recombination of $CrI_3$ and $CrBr_3$ monolayers.

hole injection and spin *e*-h recombination. From Fig. 2, the energy difference of the interlayer band gap and the spin hole injection gap between two heterostructures is only 60–80 meV, indicating that the influence of energy difference on spin hole injection and spin *e*-h recombination dynamics processes can be ignored, and the other two terms may play a vital role in determining the spin hole injection rate and spin *e*-h recombination lifetime.

To further explore the influence of *e*-ph interaction and nuclear velocity on spin hole injection and spin *e*-h recombination processes, we compute the Fourier transforms of the energy gap between key states of two heterostructures, as shown in Fig. 4. In the framework of DFT, the distribution of electronic density as well as the electronic structure and properties is determined by the positions of nuclei, according to the Kohn-Sham theorem. Thus, the variation of band gap as the function of time will be the consequence of the motion of nuclei. Mathematically, the motion of nuclei can be viewed as the supercomposition of harmonic vibrations (normal modes), and the expansion coefficients represent the contribution of the corresponding mode to the nuclei motion. In this sense, the Fourier transform on the variation of energy gap with respect to time will reveal the contribution of each mode, so as to determine the dominant phonon frequency. First, for spin hole injection and interlayer spin *e*-h recombination dynamics processes, the dominant vibrational mode at 261 $cm^{-1}$ in $CrBr_3/MoS_2$ can be assigned to the $E_g$ mode of $CrBr_3$ at ≈235 $cm^{-1}$ [65], while it shows lower-frequency modes at 39 and 121 $cm^{-1}$ in the $CrI_3/MoSe_2$ heterostructure, which can be attributed to the $E_g^1$ mode and $A_2$ mode of $CrI_3$ at 48 and 128 $cm^{-1}$, respectively [66,67]. These lower-frequency phonon modes indicate smaller nuclear velocity and result in smaller NAC, which consequently suppresses the corresponding spin carrier dynamics processes. Moreover, for intralayer spin *e*-h recombination, the situation becomes more complex. Figure 4(c) shows that some weak vibrational modes also participate in the recombination process of the $CrI_3$ and $CrBr_3$ layer and cause stronger *e*-ph coupling. Especially for $CrI_3$, the dominant vibrational mode at 121 $cm^{-1}$ disappears but some higher-frequency modes participate in *e*-ph interaction. That is, many high-frequency phonon modes largely increase the *e*-ph coupling and nuclear velocity, thus leading to faster intralayer spin *e*-h recombination comparing with $CrBr_3$. Note that the discrepancy of spectral density between the $CrI_3/MoSe_2$ heterostructure and the $CrI_3$ layer is probably attributed to the large lattice mismatch, which induces large lattice strain and markedly shifts the Raman peak position [67].

Another factor affecting the spin *e*-h recombination is the pure dephasing (decoherence), which is obtained based on the second-order cumulant approximation of the optical response theory [49]. Here we calculate the pure-dephasing function of two heterostructures and the corresponding FM layer, as shown in Fig. 5. The time constants are fitted by the Gaussian function $f(t) = \exp(-0.5(t/\tau)^2)$. In general, the faster loss of coherence means a slower quantum transition rate, as confirmed by the quantum Zeno effect [68]. Compared with that of $CrBr_3/MoS_2$, the calculated pure-dephasing time of $CrI_3/MoSe_2$ is 11.4 fs, in favor of acquiring long-lived excited spin electrons [Fig. 3(a)]. Such short-lived decoherence can be attributed to the dominant low-frequency acoustic mode at 121 $cm^{-1}$, which participates in the interlayer spin *e*-h recombination and gives rise to elastic *e*-ph scattering. In contrary, the higher-frequency optical phonon modes at 261 $cm^{-1}$ couple to the spin electrons, which leads to a slower loss of coherence (19 fs) and accelerates spin *e*-h recombination in $CrBr_3/MoS_2$. The pure-dephasing time is 27 fs for $CrI_3$ and 11.1 fs for $CrBr_3$. This can be easily understood since many more high-frequency modes participate in the intralayer spin *e*-h recombination in $CrI_3$ as compared with those in $CrBr_3$. Note that here we only focus on discussing the decoherence effect on spin *e*-h recombination dynamics process. This is because the decoherence can be ignored during the rapid relaxation along the quasicontinuous manifold of excited electronic states; oppositely, the decoherence effect is very important for slow *e*-h recombination dynamics process since the quantum-classical method generally overestimates the recombination time [47].

### D. Spin carrier mobility

Given the potential application in spintronic devices, high spin carrier mobility is another essential aspect to acquire superior spin transport. Based on the effective mass

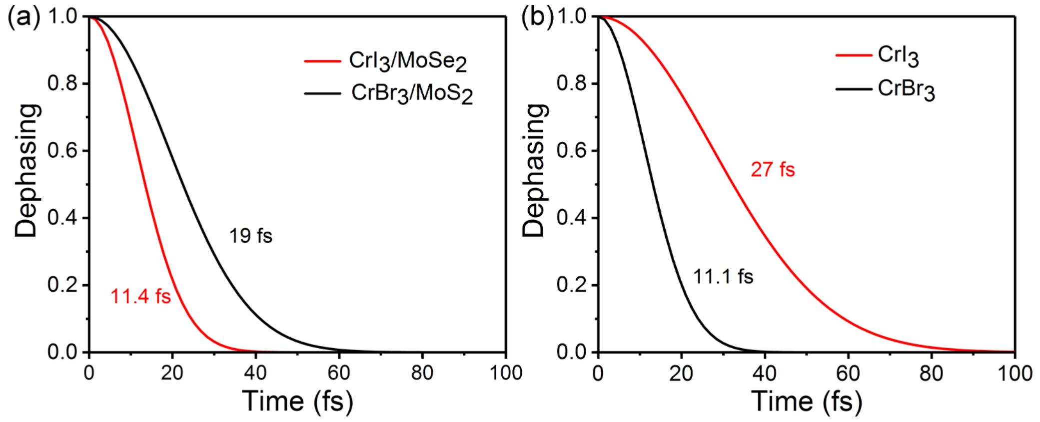


FIG. 5. Pure-dephasing functions of (a) interlayer spin *e*-h recombination and (b) intralayer spin *e*-h recombination. The time data are fitted by the Gaussian function $f(t) = \exp(-0.5(t/\tau)^2)$.

approximation, the carrier mobility is determined by the formula

$$\mu = \frac{2e\hbar^3 C}{3k_B T |m^*|^2 E_1^2}, \quad (2)$$

where $e$ is the electron charge, $C$ is the in-plane stiffness, $k_B$ is the Boltzmann constant, $T$ is the temperature, $m^*$ is the carrier effective mass, and $E_1$ is the deformation potential. The effective masses of electron ($m_e^*$) and hole ($m_h^*$) are calculated by $\hbar^2[\partial^2 E_k/\partial k^2]^{-1}$, where $k$ is the wave vector, and $E_k$ is the energy corresponding to the wave vector. The in-plane stiffness, $C = [\partial^2 E/\partial \varepsilon^2]/S_0$, is obtained by fitting the energy-strain curves (see Figs. S4(a) and S4(b) of the Supplemental Material [56]). Here $E$ is the total energy of the supercell, $\varepsilon$ is the applied uniaxial strain, and $S_0$ is the area of supercell. The deformation potential $E_1$ is calculated by $dE_{\mathrm{edge}}/d\delta$, where $E_{\mathrm{edge}}$ is the energy of CBM and VBM (see Figs. S4(c) and S4(d) of the Supplemental Material [56]). The calculated $C$, $E_1$, $m_e^*$, and $m_h^*$ along specific directions (see inset in Fig. S4(a) of the Supplemental Material [56]) are listed in Table I. The direction-dependent $m_e^*$ and $m_h^*$ indicate a distinct anisotropic character of spin carrier transport for both heterostructures. Utilizing the calculated $E_1$, $C$, and $m^*$, the hole mobility can be obtained and it is one to two orders of magnitude larger than electron mobility for $CrI_3/MoSe_2$ and this discrepancy is up to three orders of magnitude for $CrBr_3/MoS_2$. Such large hole mobility and strong anisotropy strongly facilitate the high-speed spin hole transport in these two heterostructures.

### E. Discussion

Now we will make a comparison between $CrI_3/MoSe_2$ and $CrBr_3/MoS_2$ in terms of electronic structure, spin hole injection, spin *e*-h recombination, and spin carrier mobility. According to the above analyses, we infer that the $CrBr_3/MoS_2$ heterostructure shows better performance in utilizing photogenerated fully spin-polarized current than the $CrI_3/MoSe_2$ heterostructure. This can be attributed to two aspects: on the one hand, both of them exhibit fast spin hole injection and an ultraslow interlayer spin *e*-h recombination dynamics process, which facilitates to generate long-lived spin-polarized current. However, for $CrI_3/MoSe_2$, the intralayer spin carrier recombination is much faster than that of $CrBr_3/MoS_2$. It means that when the spin carriers are excited, the photogenerated spin electrons tend to recombine with spin holes in the $CrI_3$ layer, resulting in a lower quantum yield of spin electrons. On the other hand, the $CrBr_3/MoS_2$ heterostructure shows much faster spin hole mobility compared with the $CrI_3/MoSe_2$ heterostructure, which significantly favors its high-speed spin hole transport.

In general, the HSE06 hybrid functional can obtain a more accurate band gap than the PBE functional. However, we expect that the impact of HSE06 correction on the photoinduced dynamics of the heterostructures is very limited due to the

TABLE I Deformation potential $E_1$, in-plane stiffness $C$, effective mass of carriers $m^*$, and carrier mobility $\mu$ along Γ-X and Γ-Y direction in $CrI_3/MoSe_2$ and $CrBr_3/MoS_2$ heterostructures at 30 K.

| | Direction | Carrier type | $E_1$ (eV) | $C$ (N/m) | $m^*(m_e)$ | $\mu$ (cm $^2$V$^{-1}$ s$^{-1}$) |
|---|---|---|---|---|---|---|
| $CrI_3/MoSe_2$ | Γ-X | *e* | −4.77 | 147.78 | 9.66 | 9.89 |
| | | h | −5.46 | 147.78 | 1.20 | 489.35 |
| | Γ-Y | *e* | −7.24 | 192.18 | 0.95 | 577.47 |
| | | h | −5.15 | 192.18 | 0.76 | 1783.26 |
| $CrBr_3/MoS_2$ | Γ-X | *e* | −8.93 | 217.86 | 3.89 | 7.80 |
| | | h | −2.22 | 217.86 | 2.88 | 2868.76 |
| | Γ-Y | *e* | −9.95 | 217.86 | 6.06 | 8.52 |
| | | h | −1.36 | 217.86 | 1.97 | 4314.74 |

large time scale difference (one to two orders of magnitude) between intralayer recombination and interlayer recombination. To assess the effect of HSE06 correction on the NAMD calculation, we take the intralayer spin *e*-h recombination in the $CrI_3/MoSe_2$ heterostructure as an example and use a scissor operator to correct the energy difference between PBE and HSE06 functionals in the NAMD calculation. As shown in Fig. S5 of the Supplemental Material [56], the intralayer spin *e*-h recombination lifetime with scissor operator correction is 190 ps, which is larger than that without correction (17 ps). However, the corrected lifetime of the intralayer recombination is still much faster than that (2588 ps) of the interlayer spin *e*-h recombination without correction by one order of magnitude. Thus, it is reasonable to avoid the expensive HSE06 correction in our dynamics simulation.

## IV. CONCLUSIONS

In summary, we have designed two prototypes of 2D FM/NM semiconductor heterostructures ($CrI_3/MoSe_2$ and $CrBr_3/MoS_2$) and demonstrated them as potential high-performance 2D semiconductor spintronic devices based on first-principles and excited state dynamics calculations. First of all, large spin-flip gaps presented in the band structures of both $CrI_3/MoSe_2$ and $CrBr_3/MoS_2$ heterostructures are in favor of generating photogenerated fully spin-polarized carriers. Meanwhile, the spin hole can be effectively injected from the FM layer to the NM layer due to their type-II spin-up channel. Second, through contact with the NM $MoY_2$ ($Y$ = S, Se) monolayer, the photogenerated spin carrier lifetime of the FM $CrX_3$ ($X$ = I, Br) has been significantly increased by one to two orders of magnitude. Such an ultralong spin carrier lifetime is originated from the small wave function overlap of donor-acceptor states and unique low-frequency vibrational modes, which results in a much smaller NAC. Finally, $CrX_3/MoY_2$ heterostructures expose superior spin hole mobility and the $CrBr_3/MoS_2$ heterostructure shows longer intralayer spin *e*-h recombination lifetime and higher spin hole mobility. Such superior spin transport and spin relaxation properties favor to acquire high information processing and storage ability, endowing its potential application prospect in spin computers or magnetic memory devices. Overall, our results provide valuable insights into the design of 2D FM semiconductors for spintronics devices with ultralong fully spin-polarized current lifetime.

## ACKNOWLEDGMENTS

This work is supported by the National Key Research and Development Program of China (Grant No. 2017YFA0204800), Natural Science Foundation of China (Grants No. 21973011 and No. 21903014), Basic Research Program of Jiangsu Province (Grant No. BK20190328), Fundamental Research Funds for the Central Universities (Grant No. 2242021K10009), and the Scientific Research Foundation of Graduate School of Southeast University (Grant No. YBPY1968). The authors thank the computational resources at the Big Data Center of SEU and National Supercomputing Center in Tianjin.

[1] M. N. Baibich, J. M. Broto, A. Fert, F. Nguyen Van Dau, F. Petroff, P. Etienne, G. Creuzet, A. Friederich, and J. Chazelas, Phys. Rev. Lett. **61**, 2472 (1988).

[2] G. Binasch, P. Grunberg, F. Saurenbach, and W. Zinn, Phys. Rev. B **39**, 4828 (1989).

[3] D. D. Awschalom and M. E. Flatte, Nat. Phys. **3**, 153 (2007).

[4] B. Endres, M. Ciorga, M. Schmid, M. Utz, D. Bougeard, D. Weiss, G. Bayreuther, and C. H. Back, Nat. Commun. **4**, 2068 (2013).

[5] J. C. Le Breton, S. Sharma, H. Saito, S. Yuasa, and R. Jansen, Nature (London) **475**, 82 (2011).

[6] K. R. Jeon, B. C. Min, A. Spiesser, H. Saito, S. C. Shin, S. Yuasa, and R. Jansen, Nat. Mater. **13**, 360 (2014).

[7] S. A. Wolf, D. D. Awschalom, R. A. Buhrman, J. M. Daughton, S. von Molnar, M. L. Roukes, A. Y. Chtchelkanova, and D. M. Treger, Science **294**, 1488 (2001).

[8] L. Guo, X. Gu, X. Zhu, and X. Sun, Adv. Mater. **31**, 1805355 (2019).

[9] H. Adachi, Nat. Phys. **11**, 707 (2015).

[10] H. Yan, Z. Feng, P. Qin, X. Zhou, H. Guo, X. Wang, H. Chen, X. Zhang, H. Wu, C. Jiang, and Z. Liu, Adv. Mater. **32**, 1905603 (2020).

[11] X. Chen, T. Yan, B. Zhu, S. Yang, and X. Cui, ACS Nano **11**, 1581 (2017).

[12] M. Gmitra and J. Fabian, Phys. Rev. B **92**, 155403 (2015).

[13] A. Avsar, D. Unuchek, J. Liu, O. L. Sanchez, K. Watanabe, T. Taniguchi, B. Ozyilmaz, and A. Kis, ACS Nano **11**, 11678 (2017).

[14] M. Battiato and K. Held, Phys. Rev. Lett. **116**, 196601 (2016).

[15] L. Cheng, X. Wang, W. Yang, J. Chai, M. Yang, M. Chen, Y. Wu, X. Chen, D. Chi, K. E. J. Goh, J. X. Zhu, H. Sun, S. Wang, J. C. W. Song, M. Battiato, H. Yang, and E. E. M. Chia, Nat. Phys. **15**, 347 (2019).

[16] J. M. Kikkawa and D. D. Awschalom, Nature (London) **397**, 139 (1999).

[17] B. Radisavljevic, A. Radenovic, J. Brivio, V. Giacometti, and A. Kis, Nat. Nanotechnol. **6**, 147 (2011).

[18] K. F. Mak, C. Lee, J. Hone, J. Shan, and T. F. Heinz, Phys. Rev. Lett. **105**, 136805 (2010).

[19] V. Nicolosi, M. Chhowalla, M. G. Kanatzidis, M. S. Strano, and J. N. Coleman, Science **340**, 1226419 (2013).

[20] W. Wu, L. Wang, Y. Li, F. Zhang, L. Lin, S. Niu, D. Chenet, X. Zhang, Y. Hao, T. F. Heinz, J. Hone, and Z. L. Wang, Nature (London) **514**, 470 (2014).

[21] A. Ramasubramaniam and D. Naveh, Phys. Rev. B **87**, 195201 (2013).

[22] B. Li, L. Huang, M. Zhong, N. Huo, Y. Li, S. Yang, C. Fan, J. Yang, W. Hu, Z. Wei, and J. Li, ACS Nano **9**, 1257 (2015).

[23] K. Zhang, S. Feng, J. Wang, A. Azcatl, N. Lu, R. Addou, N. Wang, C. Zhou, J. Lerach, V. Bojan, M. J. Kim, L. Q. Chen, R. M. Wallace, M. Terrones, J. Zhu, and J. A. Robinson, Nano Lett. **15**, 6586 (2015).

[24] B. Li, T. Xing, M. Zhong, L. Huang, N. Lei, J. Zhang, J. Li, and Z. Wei, Nat. Commun. **8**, 1958 (2017).

[25] L. Cai, J. He, Q. Liu, T. Yao, L. Chen, W. Yan, F. Hu, Y. Jiang, Y. Zhao, T. Hu, Z. Sun, and S. Wei, J. Am. Chem. Soc. **137**, 2622 (2015).
[26] Q. Chen, Y. Ouyang, S. Yuan, R. Li, and J. Wang, ACS Appl. Mater. Interfaces **6**, 16835 (2014).
[27] N. Sethulakshmi, A. Mishra, P. M. Ajayan, Y. Kawazoe, A. K. Roy, A. K. Singh, and C. S. Tiwary, Mater. Today **27**, 107 (2019).
[28] Z. Zhang, X. Zou, V. H. Crespi, and B. I. Yakobson, ACS Nano **7**, 10475 (2013).
[29] C. Zhao, Q. Zheng, J. Wu, and J. Zhao, Phys. Rev. B **96**, 134308 (2017).
[30] B. Huang, G. Clark, E. Navarro-Moratalla, D. R. Klein, R. Cheng, K. L. Seyler, D. Zhong, E. Schmidgall, M. A. McGuire, D. H. Cobden, W. Yao, D. Xiao, P. Jarillo-Herrero, and X. Xu, Nature (London) **546**, 270 (2017).
[31] Z. Zhang, J. Shang, C. Jiang, A. Rasmita, W. Gao, and T. Yu, Nano Lett. **19**, 3138 (2019).
[32] C. Gong, L. Li, Z. Li, H. Ji, A. Stern, Y. Xia, T. Cao, W. Bao, C. Wang, Y. Wang, Z. Q. Qiu, R. J. Cava, S. G. Louie, J. Xia, and X. Zhang, Nature (London) **546**, 265 (2017).
[33] B. Wang, X. Zhang, Y. Zhang, S. Yuan, Y. Guo, S. Dong, and J. Wang, Mater. Horiz. **7**, 1623 (2020).
[34] F. Ceballos, M. Z. Bellus, H. Y. Chiu, and H. Zhao, ACS Nano **8**, 12717 (2014).
[35] X. Hong, J. Kim, S. F. Shi, Y. Zhang, C. Jin, Y. Sun, S. Tongay, J. Wu, Y. Zhang, and F. Wang, Nat. Nanotechnol. **9**, 682 (2014).
[36] H. Chen, X. Wen, J. Zhang, T. Wu, Y. Gong, X. Zhang, J. Yuan, C. Yi, J. Lou, P. M. Ajayan, W. Zhuang, G. Zhang, and J. Zheng, Nat. Commun. **7**, 12512 (2016).
[37] C. Jin, E. Y. Ma, O. Karni, E. C. Regan, F. Wang, and T. F. Heinz, Nat. Nanotechnol. **13**, 994 (2018).
[38] R. Long and O. V. Prezhdo, Nano Lett. **16**, 1996 (2016).
[39] Q. Zheng, W. A. Saidi, Y. Xie, Z. Lan, O. V. Prezhdo, H. Petek, and J. Zhao, Nano Lett. **17**, 6435 (2017).
[40] Q. Zheng, W. Chu, C. Zhao, L. Zhang, H. Guo, Y. Wang, X. Jiang, and J. Zhao, WIREs Comput. Mol. Sci. **9**, e1411 (2019).
[41] G. Kresse and J. Furthmuller, Phys. Rev. B **54**, 11169 (1996).
[42] G. Kresse and J. Furthmuller, Comput. Mater. Sci. **6**, 15 (1996).
[43] J. P. Perdew, K. Burke, and M. Ernzerhof, Phys. Rev. Lett. **77**, 3865 (1996).
[44] G. Kresse and D. Joubert, Phys. Rev. B **59**, 1758 (1999).
[45] S. Grimme, J. Antony, S. Ehrlich, and H. Krieg, J. Chem. Phys. **132**, 154104 (2010).
[46] J. Paier, M. Marsman, K. Hummer, G. Kresse, I. C. Gerber, and J. G. Angyan, J. Chem. Phys. **124**, 154709 (2006).
[47] A. V. Akimov and O. V. Prezhdo, J. Chem. Theory Comput. **10**, 789 (2014).
[48] A. V. Akimov and O. V. Prezhdo, J. Chem. Theory Comput. **9**, 4959 (2013).
[49] H. M. Jaeger, S. Fischer, and O. V. Prezhdo, J. Chem. Phys. **137**, 22A545 (2012).
[50] X. Li and J. Yang, Natl. Sci. Rev. **3**, 365 (2016).
[51] L. Webster and J. A. Yan, Phys. Rev. B **98**, 144411 (2018).
[52] Y. Guo, S. Yuan, B. Wang, L. Shi, and J. Wang, J. Mater. Chem. C **6**, 5716 (2018).
[53] Y. Zhao, J. J. Zhang, S. Yuan, and Z. Chen, Adv. Funct. Mater. **29**, 1901420 (2019).
[54] H. Zhang, Y. Ning, W. Yang, J. Zhang, R. Zhang, and X. Xu, Phys. Chem. Chem. Phys. **21**, 17087 (2019).
[55] Q. Shao, G. Yu, Y. W. Lan, Y. Shi, M. Y. Li, C. Zheng, X. Zhu, L. J. Li, P. K. Amiri, and K. L. Wang, Nano Lett. **16**, 7514 (2016).
[56] See Supplemental Material at http://link.aps.org/supplemental/10.1103/PhysRevB.103.245411 for band structure, state population, and carrier mobility of $CrI_3/MoSe_2$ and $CrBr_3/MoS_2$ heterostructures.
[57] V. O. Özçelik, J. G. Azadani, C. Yang, S. J. Koester, and T. Low, Phys. Rev. B **94**, 035125 (2016).
[58] R. Zhang, L. Zhang, Q. Zheng, P. Gao, J. Zhao, and J. Yang, J. Phys. Chem. Lett. **9**, 5419 (2018).
[59] Z. Zhou, X. Niu, Y. Zhang, and J. Wang, J. Mater. Chem. A **7**, 21835 (2019).
[60] L. Li, R. Long, and O. V. Prezhdo, Chem. Mater. **29**, 2466 (2016).
[61] Y. Yang, W. H. Fang, and R. Long, J. Phys. Chem. Lett. **8**, 5771 (2017).
[62] H. Guo, C. Zhao, Q. Zheng, Z. Lan, O. V. Prezhdo, W. A. Saidi, and J. Zhao, J. Phys. Chem. Lett. **9**, 3485 (2018).
[63] L. Zhang, Q. Zheng, Y. Xie, Z. Lan, O. V. Prezhdo, W. A. Saidi, and J. Zhao, Nano Lett. **18**, 1592 (2018).
[64] K. G. Reeves, A. Schleife, A. A. Correa, and Y. Kanai, Nano Lett. **15**, 6429 (2015).
[65] V. M. Bermudez, Solid State Commun. **19**, 693 (1976).
[66] Y. Zhang, X. Wu, B. Lyu, M. Wu, S. Zhao, J. Chen, M. Jia, C. Zhang, L. Wang, X. Wang, Y. Chen, J. Mei, T. Taniguchi, K. Watanabe, H. Yan, Q. Liu, L. Huang, Y. Zhao, and M. Huang, Nano Lett. **20**, 729 (2019).
[67] D. T. Larson and E. Kaxiras, Phys. Rev. B **98**, 085406 (2018).
[68] S. V. Kilina, A. J. Neukirch, B. F. Habenicht, D. S. Kilin, and O. V. Prezhdo, Phys. Rev. Lett. **110**, 180404 (2013).